

Modeling photocurrent action spectra of photovoltaic devices based on organic thin films

Leif A. A. Pettersson,^{a)} Lucimara S. Roman, and Olle Inganäs
Department of Physics and Measurement Technology, Linköping University, S-581 83 Linköping, Sweden

(Received 27 October 1998; accepted for publication 25 February 1999)

We have modeled experimental short-circuit photocurrent action spectra of poly(3-(4'-(1'',4'',7''-trioxaocetyl)phenyl)thiophene) (PEOPT)/fullerene (C_{60}) thin film heterojunction photovoltaic devices. Modeling was based on the assumption that the photocurrent generation process is the result of the creation and diffusion of photogenerated species (excitons), which are dissociated by charge transfer at the PEOPT/ C_{60} interface. The internal optical electric field distribution inside the devices was calculated with the use of complex indices of refraction and layer thickness of the materials as determined by spectroscopic ellipsometry. Contributions to the photocurrent from optical absorption in polymer and fullerene layers were both necessary to model the experimental photocurrent action spectra. We obtained values for the exciton diffusion range of 4.7 and 7.7 nm for PEOPT and C_{60} , respectively. The calculated internal optical electric field distribution and resulting photocurrent action spectra were used in order to study the influence of the geometrical structure with respect to the efficiency of the thin film devices. In this way the photocurrent was optimized. © 1999 American Institute of Physics. [S0021-8979(99)05113-0]

I. INTRODUCTION

Organic thin film photovoltaic devices based on conjugated molecules and polymers have been shown to be highly efficient.¹⁻³ The high conversion efficiencies are the result of efficient absorption of light and charge generation inside the devices. While photovoltaic devices of a single active conjugated polymer layer in general exhibit low efficiency of energy conversion, blends and heterojunctions (bilayers) with molecules having high electron affinity and low ionization potential considerably enhance the efficiency. Although presently the subject of some controversy, the mechanism for generation of photocurrent in organic thin film photovoltaic devices is believed to be due to the creation of bound electron-hole pairs, excitons, by absorption of light in the active parts of the devices. Charge generation occurs as a result of dissociation of the excitons by interaction of the excitons with interfaces, impurities or defects, or in high electrical fields. The incorporation of dissociation sites is thus the reason for the higher efficiency of devices made of blends and bilayers. In the case of thin film photodiodes, a number of layers are stacked on top of each other in a multilayer configuration. Reflections at interfaces affect the distribution of the optical electric field inside the thin film photodiodes. The generation of excitons is directly dependent on the distribution of the optical electric field energy dissipation, which consequently will influence the photocurrent action spectra of the devices. For that reason the distribution of the optical electric field energy inside the device is an important aspect to consider in studying and determining device properties.

A number of studies have employed different models to describe the photovoltaic action spectra.⁴⁻⁹ Harrison, Grüner,

and Spencer give a thorough description of some of these models.¹⁰ Common for the models is the assumption that the intensity of the optical electric field is considered to have an exponential decrease along the direction of propagation inside the device structure. Effects such as reflections and interference are neglected. These effects become especially important for thin film structures where layers are thin compared to the penetration depth and/or the wavelength of the incident light, and also in the case of a highly reflecting interface present inside the device, as, for example, in the case of the metal electrodes normally used in photovoltaic devices.

We report our attempts to model the experimental photocurrent action spectrum of thin film organic photovoltaic devices concentrating on a donor-acceptor heterojunction between a conjugated polymer and fullerene (C_{60}), a configuration which has previously been investigated.^{1,11-13} In order to model the experimental photocurrent action spectra, we extracted optical properties in terms of the complex index of refraction as well as layer thickness by analysis of spectroscopic ellipsometry data. These were then used in the proper calculation of the optical electric field distribution inside the device. From this distribution, we are able to calculate the distribution of optical absorption in the device layers. Assuming that charge generation occurs at the poly(3-(4'-(1'',4'',7''-trioxaocetyl)phenyl)thiophene) (PEOPT)/ C_{60} interface, we can integrate this distribution into a diffusion equation for excitons in the device, and predict the photocurrent density and quantum efficiency. Since the efficiency of the device is dependent on the distribution of the internal optical electric field, geometrical aspects are important for enhancing the efficiency of the device. We can also extract the diffusion length of excitons in PEOPT and C_{60} layers within this model.

^{a)}Electronic mail: lpe@ifm.liu.se

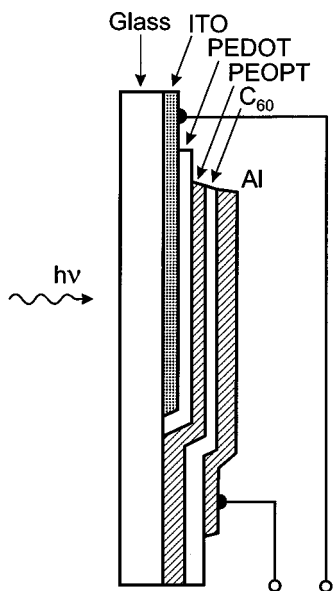


FIG. 1. Schematic presentation of the thin film photovoltaic device structure: glass/ITO/PEDOT/PEOPT/ C_{60} /Al.

In addition, the distribution of the excited species due to the optical electric field is given as an analytical expression. This distribution has not only implications for photovoltaic devices, but also describes the distribution of excited states for radiative decay of photoluminescence in layered media.

In Sec. II we describe experimental details, followed by a theory section describing the theory of the photocurrent generation model (Sec. III). This is divided into three parts: assumptions used in the model, the treatment of the internal optical electric field and the energy dissipation due to an incident plane wave in layered media, and the exciton transport described by the diffusion equation. In Sec. IV, model and experimental results are presented and discussed.

II. EXPERIMENTAL DETAILS

The organic heterojunction photovoltaic devices studied in this work were of the thin film (sandwich) structure type as shown schematically in Fig. 1. The device consisted of a poly(3,4-ethylenedioxythiophene)-poly(styrenesulfonate) (PEDOT-PSS), see Fig. 2, (Baytron-Bayer AG) layer spin coated onto an indium tin oxide (ITO)/glass substrate as hole collecting electrode and Al as electron collecting electrode. The PEDOT-PSS layer is used due to the fact that the injection/collection conditions for electrons/holes are much better for the PEDOT-PSS/PEOPT interface compared to the ITO/PEOPT interface resulting in improved current-voltage characteristics of the device. The donor-acceptor heterojunction is built up by poly(3-(4'-(1'',4'',7''-trioxaoctyl)phenyl)thiophene) (PEOPT), see Fig. 2, and C_{60} (TechnoCarbon, 99%). The polymer layer was spin coated from a 5 mg/ml chloroform solution and the C_{60} layer was sublimed on top of the polymer. The current-voltage characteristics and the quantum efficiency of this device have been reported previously, where a more detailed description of the device preparation was given.¹ Measurements of the photocurrent were performed with a Keithley 485 picoammeter during

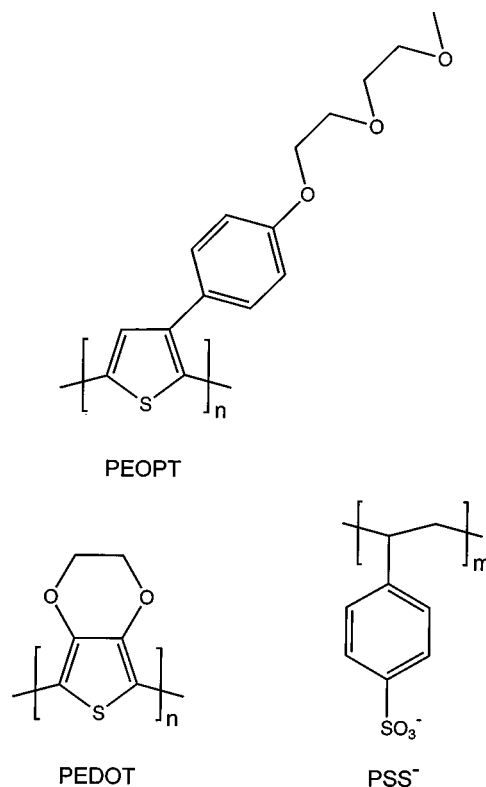


FIG. 2. Chemical structures of poly(3-(4'-(1'',4'',7''-trioxaoctyl)phenyl)thiophene) (PEOPT), poly(3,4-ethylenedioxythiophene) (PEDOT), and poly(styrenesulfonate) anion (PSS^-).

illumination of the device through the glass/ITO side with monochromatic light from an MS 257 Oriel monochromator and a tungsten-halogen lamp. The intensity of the light was measured using a calibrated silicon photodiode at the same position as the samples.

The complex index of refraction, $\tilde{n} = \eta + i\kappa$, of each material and the thickness of each layer are needed in the modeling of the photocurrent action spectra and were determined by analysis of spectroscopic ellipsometry data. Ellipsometric data were acquired with a rotating analyzer NIR-VIS-UV variable-angle spectroscopic ellipsometer (J. A. Woollam Co., Inc.). Measurements were performed at multiple angles of incidence on separate layers of the materials. In order to relate the measured ellipsometry data to the actual material characteristics in terms of the complex index of refraction, a numerical data analysis must be performed. In this analysis, the complex index of refraction and the thickness of the layers were varied to obtain a best fit between model and experimental ellipsometry data.¹⁴

III. THEORY

A. Photocurrent generation model

The primary process for generation of photocurrent in an organic photovoltaic device is the generation of bound electron-hole pairs (excitons) by absorption of energy (photons) from the optical electric field. Once created, the exciton has a lifetime determined by recombination through radiative or nonradiative decay or by dissociation into free charge carriers. The desired process, to make charge collection pos-

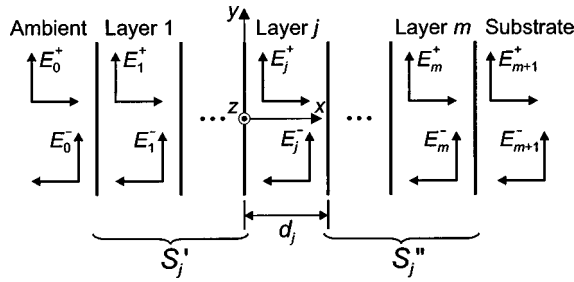


FIG. 3. A general multilayer structure having m layers between a semi-infinite transparent ambient and a semi-infinite substrate. Each layer j ($j = 1, 2, \dots, m$) has a thickness d_j and its optical properties are described by its complex index of refraction. The optical electric field at any point in layer j is represented by two components: one propagating in the positive and one in the negative x direction, \mathbf{E}_j^+ and \mathbf{E}_j^- , respectively.

sible, is the dissociation of the exciton into free charge carriers. The dissociation can be forced by an electric field or by interaction of the excitons with interfaces, impurities, or defects where charge transfer can occur. Since the diffusion range of the excitons is limited, only those excitons within a diffusion range of the dissociation sites will contribute to the photocurrent. Our model in principle follows the model of Ghosh and Feng,⁴ where the exciton diffusion is described by the standard diffusion equation. However, in our case the model is extended to take into account the distribution of the total exciting optical electric field inside the thin film structure. Assumptions in our model are that (1) layers included in the device are considered to be homogeneous and isotropic, so that their linear optical response can be described by a scalar complex index of refraction; (2) interfaces are parallel and flat compared to the wavelength of the light; and (3) the light incident at the device can be described by plane waves. (4) Exciton diffusion is described by the diffusion equation [see Eq. (26)] and (5) those excitons that contribute to the photocurrent dissociate into charge carriers at interfaces that act as dissociation sites; (6) the diffusion range of excitons is not dependent on excitation energy (wavelength), and finally (7) that all generated charges are contributing to the steady state photocurrent, i.e., no trapping of charges occurs inside the device.

B. Internal optical electric field and energy dissipation due to an incident plane wave

When considering stratified media in terms of the electromagnetic theory of light, many different approaches are possible in order to obtain the reflection and transmission coefficient of the electromagnetic field. One of the more elegant approaches for multilayer structures is to employ matrix methods. Stratified structures with isotropic and homogeneous media and parallel-plane interfaces can be described by 2×2 matrices due to the fact that the equations governing the propagation of the electric field are linear and that the tangential component of the electric field is continuous.^{15,16}

Consider a plane wave incident from left at a general multilayer structure having m layers between a semi-infinite transparent ambient and a semi-infinite substrate as schematically described in Fig. 3. Each layer j ($j = 1, 2, \dots, m$) has a thickness d_j and its optical properties are described by its

complex index of refraction $\tilde{n}_j = \eta_j + i\kappa_j$ (or complex dielectric function $\tilde{\epsilon}_j = \epsilon'_j + i\epsilon''_j = \tilde{n}_j^2$) which is a function of wavelength (energy) of the incident light. The optical electric field at any point in the system can be resolved into two components corresponding to the resultant total electric field; one component propagating in the positive x direction and one in the negative x direction, which at a position x in layer j are denoted $\mathbf{E}_j^+(x)$ and $\mathbf{E}_j^-(x)$, respectively. An interface matrix (matrix of refraction) then describes each interface in the structure

$$I_{jk} = \frac{1}{t_{jk}} \begin{bmatrix} 1 & r_{jk} \\ r_{jk} & 1 \end{bmatrix}, \quad (1)$$

where r_{jk} and t_{jk} are the Fresnel complex reflection and transmission coefficients at interface jk . For light with the electric field perpendicular to the plane of incidence (s -polarized or TE waves) the Fresnel complex reflection and transmission coefficients are defined by

$$r_{jk} = \frac{q_j - q_k}{q_j + q_k}, \quad (2a)$$

$$t_{jk} = \frac{2q_j}{q_j + q_k} \quad (2b)$$

and for light with the electric field parallel to the plane of incidence (p -polarized or TM waves) as

$$r_{jk} = \frac{\tilde{n}_k^2 q_j - \tilde{n}_j^2 q_k}{\tilde{n}_k^2 q_j + \tilde{n}_j^2 q_k}, \quad (3a)$$

$$t_{jk} = \frac{2\tilde{n}_j \tilde{n}_k q_j}{\tilde{n}_k^2 q_j + \tilde{n}_j^2 q_k}, \quad (3b)$$

where

$$q_j = \tilde{n}_j \cos \phi_j = [\tilde{n}_j^2 - \eta_0^2 \sin^2 \phi_0]^{1/2} \quad (4)$$

and η_0 is the refractive index of the transparent ambient, ϕ_0 is the angle of incidence, and ϕ_j is the angle of refraction in layer j . The layer matrix (phase matrix) describing the propagation through layer j is described by

$$L_j = \begin{bmatrix} e^{-i\xi_j d_j} & 0 \\ 0 & e^{i\xi_j d_j} \end{bmatrix}, \quad (5)$$

where

$$\xi_j = \frac{2\pi}{\lambda} q_j \quad (6)$$

and $\xi_j d_j$ is the layer phase thickness corresponding to the phase change the wave experiences as it traverses layer j . By using the interface matrix and the layer matrix of Eqs. (1) and (5) the total system transfer matrix (scattering matrix) \mathbf{S} , which relates the electric field at ambient side and substrate side by

$$\begin{bmatrix} \mathbf{E}_0^+ \\ \mathbf{E}_0^- \end{bmatrix} = \mathbf{S} \begin{bmatrix} \mathbf{E}_{m+1}^+ \\ \mathbf{E}_{m+1}^- \end{bmatrix}, \quad (7)$$

can be written

$$\mathbf{S} = \begin{bmatrix} S_{11} & S_{12} \\ S_{21} & S_{22} \end{bmatrix} = \left(\prod_{v=1}^m \mathbf{I}_{(v-1)v} \mathbf{L}_v \right) \cdot \mathbf{I}_{m(m+1)}. \quad (8)$$

When light is incident from the ambient side in the positive x direction there is no wave propagating in the negative x direction inside the substrate, which means that $\mathbf{E}_{m+1}^- = 0$. For the total layered structure the resulting complex reflection and transmission coefficients can be expressed by using the matrix elements of the total system transfer matrix of Eq. (8) as

$$r = \frac{\mathbf{E}_0^-}{\mathbf{E}_0^+} = \frac{S_{21}}{S_{11}}, \quad (9)$$

$$t = \frac{\mathbf{E}_{m+1}^+}{\mathbf{E}_0^+} = \frac{1}{S_{11}}. \quad (10)$$

In order to calculate the internal electric field in layer j the layer system can be divided into two subsets, separated by layer j , which means that the total system transfer matrix can be written as

$$\mathbf{S} = \mathbf{S}'_j \mathbf{L}_j \mathbf{S}''_j. \quad (11)$$

The partial system transfer matrices for layer j (Fig. 3) are defined

$$\begin{bmatrix} \mathbf{E}_0^+ \\ \mathbf{E}_0^- \end{bmatrix} = \mathbf{S}'_j \begin{bmatrix} \mathbf{E}_j^+ \\ \mathbf{E}_j^- \end{bmatrix}, \quad (12)$$

$$\mathbf{S}'_j = \begin{bmatrix} S'_{j11} & S'_{j12} \\ S'_{j21} & S'_{j22} \end{bmatrix} = \left(\prod_{v=1}^{j-1} \mathbf{I}_{(v-1)v} \mathbf{L}_v \right) \cdot \mathbf{I}_{(j-1)j},$$

where \mathbf{E}_j^+ and \mathbf{E}_j^- refer to the left boundary $(j-1)j$ of layer j and

$$\begin{bmatrix} \mathbf{E}_j^{''+} \\ \mathbf{E}_j^{''-} \end{bmatrix} = \mathbf{S}''_j \begin{bmatrix} \mathbf{E}_{m+1}^+ \\ \mathbf{E}_{m+1}^- \end{bmatrix}, \quad (13)$$

$$\mathbf{S}''_j = \begin{bmatrix} S''_{j11} & S''_{j12} \\ S''_{j21} & S''_{j22} \end{bmatrix} = \left(\prod_{v=j+1}^m \mathbf{I}_{(v-1)v} \mathbf{L}_v \right) \cdot \mathbf{I}_{m(m+1)},$$

where $\mathbf{E}_j^{''+}$ and $\mathbf{E}_j^{''-}$ refer to the right boundary $j(j+1)$ of layer j . Also for the partial systems \mathbf{S}'_j and \mathbf{S}''_j , it is possible to define complex reflection and transmission coefficients for layer j in terms of the matrix elements

$$r'_j = \frac{S'_{j21}}{S'_{j11}}, \quad (14)$$

$$t'_j = \frac{1}{S'_{j11}}, \quad (15)$$

$$r''_j = \frac{S''_{j21}}{S''_{j11}}, \quad (16)$$

$$t''_j = \frac{1}{S''_{j11}}. \quad (17)$$

Combining Eqs. (9)–(17) an internal transfer coefficient which relates the incident plane wave to the internal electric field propagating in the positive x direction in layer j at interface $(j-1)j$ can be derived as

$$t_j^+ = \frac{\mathbf{E}_j^+}{\mathbf{E}_0^+} = \frac{t'_j}{1 - r'_j - r''_j \cdot e^{i2\xi_j d_j}}, \quad (18)$$

where $r'_{j-} = -S'_{j12}/S'_{j11}$. An internal transfer coefficient which relates the incident plane wave to the internal electric field propagating in the negative x direction in layer j at interface $(j-1)j$ can also be derived as

$$t_j^- = \frac{\mathbf{E}_j^-}{\mathbf{E}_0^+} = \frac{t'_j r''_j \cdot e^{i2\xi_j d_j}}{1 - r'_{j-} r''_j \cdot e^{i2\xi_j d_j}} = t_j^+ r''_j \cdot e^{i2\xi_j d_j}. \quad (19)$$

With use of Eqs. (18) and (19) the total electric field in an arbitrary plane in layer j at a distance x to the right of boundary $(j-1)j$ in terms of the incident plane wave \mathbf{E}_0^+ is given by

$$\begin{aligned} \mathbf{E}_j(x) &= \mathbf{E}_j^+(x) + \mathbf{E}_j^-(x) \\ &= [t_j^+ e^{i\xi_j x} + t_j^- e^{-i\xi_j x}] \mathbf{E}_0^+ \\ &= t_j^+ [e^{i\xi_j x} + r''_j e^{i\xi_j (2d_j - x)}] \mathbf{E}_0^+ \end{aligned} \quad (20)$$

for $0 \leq x \leq d_j$. The expression in Eq. (20) can also be expressed in terms of the matrix elements of the partial system transfer matrices as

$$\mathbf{E}_j(x) = \frac{S''_{j11} \cdot e^{-i\xi_j (d_j - x)} + S''_{j21} \cdot e^{i\xi_j (d_j - x)}}{S'_{j11} S''_{j11} \cdot e^{-i\xi_j d_j} + S'_{j12} S''_{j21} \cdot e^{i\xi_j d_j}} \mathbf{E}_0^+. \quad (21)$$

Since the number of excited states at a given position in a structure is directly dependent on the energy absorbed by the material, the energy dissipation of the electromagnetic field in the material is the quantity that is of interest in the case of photovoltaic devices. The time average of the energy dissipated per second in layer j at position x at normal incidence is given by (c , speed of light; ϵ_0 , permittivity of free space)

$$Q_j(x) = \frac{1}{2} c \epsilon_0 \alpha_j \eta_j |\mathbf{E}_j(x)|^2. \quad (22)$$

This means that the energy absorbed at position x in the layered structure is proportional to the product of the modulus squared of the electric field $|\mathbf{E}_j(x)|^2$, the refractive index η_j , and the absorption coefficient

$$\alpha_j = \frac{4\pi\kappa_j}{\lambda} \quad (23)$$

at the actual position x . Thus, the number of excited states in a layer is proportional to the number of absorbed photons and, hence, $|\mathbf{E}|^2$ versus position x in the film directly represents the production of excited states at each point. Expanding Eq. (22) with the use of Eq. (20), the result for light incident at normal incidence becomes

$$\begin{aligned} Q_j(x) &= \alpha_j T_j I_0 \left[e^{-\alpha_j x} + \rho_j^{n2} \cdot e^{-\alpha_j (2d_j - x)} + 2\rho_j'' \cdot e^{-\alpha_j d_j} \right. \\ &\quad \left. \cdot \cos\left(\frac{4\pi\eta_j}{\lambda}(d_j - x) + \delta_j''\right) \right], \end{aligned} \quad (24)$$

where I_0 is the intensity of the incident light, $T_j = (\eta_j/\eta_0)|t_j^+|^2$ is the internal intensity transmittance, and ρ_j^n and δ_j^n are the absolute value and the argument of the complex reflection coefficient for the second subsystem given by Eq. (16). As can be seen in Eq. (24), the energy dissipation in a layered structure at each position x in layer j is described by three terms. The first term on the right originates from the optical electric field propagating in the positive x direction,

(the same direction as the incident electromagnetic field is propagating), the second from the field propagating in the negative x direction, and the third is due to interference of the two waves. This interference term becomes especially important for optically thin layers and when the layered structure has a highly reflecting interface in the structure, as, for example, in the case of metal electrodes in the device described in this work. The distribution of the optical electric field [Eq. (24)] is also of importance in photoluminescence studies of radiative decay in layered media. The distribution of the optical electric field is directly related to the distribution of the excited states in the device and thus describes the excitation profile in a layered structure.

We note that with other models⁴⁻⁹ the generation of excitons or carriers has been described by an excitation profile corresponding to

$$Q(x) = \alpha I_0 e^{-\alpha x}. \tag{25}$$

In this expression, reflection at the front surface of the device and the optical mode structure inside the device are neglected and will therefore only give an approximate description in the case of a single layer that is thick compared to the penetration depth of light, $1/\alpha$, of the material. In the case of a thin film photovoltaic device the situation is more complex and Eq. (24) is for that reason a better description of the generation of excited species in the active regions of the photovoltaic device.

In the model calculations of our actual device structure special care must be taken to the transparent glass substrate. The transmission of a beam of light through the glass must, due to the large thickness (1 mm) and nonuniformity in the thickness of the glass, and the finite bandwidth of the light source, be treated as being incoherent with respect to other beams. This was in this work accomplished by calculating the resultant transmission through the glass substrate by summation of transmitted energies (intensities) instead of complex amplitudes.

In the following section all the equations and parameters refer to one layer and hence the index j will be dropped.

C. Exciton transport—diffusion equation

Consider photogenerated excitons formed by photoexcitation within an active layer. The excitons can diffuse from the position where they were created and be dissociated by

interaction of the exciton at interfaces, impurities or defects. After the dissociation of the exciton, charge collection is possible. If n is the exciton density the diffusion equation gives

$$\frac{\partial n}{\partial t} = D \frac{\partial^2 n}{\partial x^2} - \frac{n}{\tau} + \frac{\theta_1}{h\nu} Q(x), \tag{26}$$

where D is the diffusion constant, τ is the mean lifetime of the exciton, θ_1 is the quantum efficiency of the exciton generation, and $h\nu$ is the excitation energy of the incident light. In Eq. (26) the first term on the right represents excitons moving away by diffusion, the second term is a recombination term, and the third term represents the generation rate of excitons (photogeneration). At steady state (equilibrium), the exciton density is time independent and Eq. (26) can be written as

$$\frac{d^2 n}{dx^2} = \beta^2 n(x) - \frac{\theta_1}{D h\nu} Q(x), \tag{27}$$

where $\beta = 1/L = 1/\sqrt{D\tau}$, i.e., the reciprocal of the diffusion length L . The general solution to Eq. (27) with the generation term as given by Eq. (24) is

$$n(x) = \frac{\theta_1 \alpha TN}{D(\beta^2 - \alpha^2)} \left[A \cdot e^{-\beta x} + B \cdot e^{\beta x} + e^{-\alpha x} + C_1 \cdot e^{\alpha x} + C_2 \cdot \cos\left(\frac{4\pi\eta}{\lambda}(d-x) + \delta''\right) \right], \tag{28}$$

where N is the number of incident photons at the device per unit time per unit area (incident photon flux). A and B are constants given by the boundary condition in the model and

$$C_1 = \rho^{n2} e^{-2\alpha d}, \tag{29}$$

$$C_2 = \frac{(\beta^2 - \alpha^2)}{(\beta^2 + (4\pi\eta/\lambda)^2)} 2\rho'' e^{-\alpha d}. \tag{30}$$

Assuming that the interfaces of the active layer act as perfect sinks for the excitons, i.e., all excitons can either recombine or dissociate into free charges at the interfaces resulting in boundary conditions $n=0$ at $x=0$ and $x=d$. Solving for the two constants A and B using these boundary conditions together with Eq. (28), the result becomes

$$A = \frac{(e^{\beta d} - e^{-\alpha d}) + C_1(e^{\beta d} - e^{\alpha d}) + C_2 \left[e^{\beta d} \cdot \cos\left(\frac{4\pi\eta}{\lambda}d + \delta''\right) - \cos(\delta'') \right]}{(e^{-\beta d} - e^{\beta d})} \tag{31}$$

and

$$B = - \frac{(e^{-\beta d} - e^{-\alpha d}) + C_1(e^{-\beta d} - e^{\alpha d}) + C_2 \left[e^{-\beta d} \cdot \cos\left(\frac{4\pi\eta}{\lambda}d + \delta''\right) - \cos(\delta'') \right]}{(e^{-\beta d} - e^{\beta d})}. \tag{32}$$

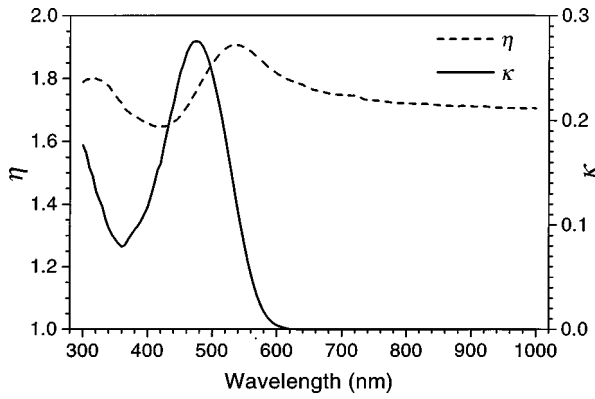


FIG. 4. Complex index of refraction $\tilde{n} = \eta + i\kappa$ of poly(3-(4'-(1'',4'',7''-trioxaoctyl)phenyl)thiophene) (PEOPT) in the wavelength range 300–1000 nm (1.24–5.00 eV).

The short-circuit exciton current density at the interface $x = 0$ can be found as

$$J_{\text{Exc}} = D \left. \frac{dn}{dx} \right|_{x=0}, \quad (33)$$

which is related to the short-circuit photocurrent through $J_{\text{Photo}} = q\theta_2 J_{\text{Exc}}$, where q is the electron charge and θ_2 is the efficiency of the exciton dissociation at the interface. The resulting short-circuit photocurrent density generated at this interface therefore is

$$J_{\text{Photo}}|_{x=0} = \frac{q\theta\alpha TN}{(\beta^2 - \alpha^2)} \left(-\beta A + \beta B - \alpha + \alpha C_1 + \frac{4\pi\eta}{\lambda} C_2 \cdot \sin \left[\frac{4\pi\eta}{\lambda} d + \delta'' \right] \right), \quad (34)$$

where the total quantum efficiency of the free charge generation is defined as $\theta = \theta_1\theta_2$. In the same way for interface $x = d$ the short-circuit exciton current density can be found as

$$J_{\text{Exc}} = -D \left. \frac{dn}{dx} \right|_{x=d} \quad (35)$$

resulting with the generated short-circuit photocurrent density as

$$J_{\text{Photo}}|_{x=d} = \frac{q\theta\alpha TN}{(\beta^2 - \alpha^2)} \left(\beta A \cdot e^{-\beta d} - \beta B \cdot e^{\beta d} + \alpha \cdot e^{-\alpha d} - \alpha C_1 \cdot e^{\alpha d} - \frac{4\pi\eta}{\lambda} C_2 \cdot \sin[\delta''] \right). \quad (36)$$

From Eqs. (34) and (36) it is seen that the generated photocurrent is directly proportional to the intensity of the incident light at the photovoltaic device, since the intensity of the incident light, I_0 , is related to the incident photon flux through, $I_0 = h\nu N$.

IV. EXPERIMENTAL RESULTS AND DISCUSSION

Optical functions as determined from spectroscopic ellipsometry data analysis of the active materials in the photovoltaic device, i.e., the PEOPT and C_{60} , are presented in Figs. 4 and 5, respectively. These data, together with optical

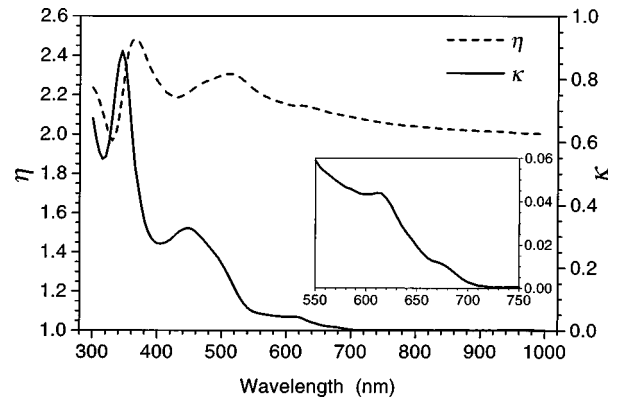


FIG. 5. Complex index of refraction $\tilde{n} = \eta + i\kappa$ of C_{60} in the wavelength range 300–1000 nm (1.24–5.00 eV). The inset shows a magnification of the extinction coefficient in the wavelength range 550–750 nm.

functions of the other materials included in the photovoltaic device, were used in the modeling of the experimental photocurrent action spectra. The absorption coefficients of PEOPT and C_{60} in the wavelength range corresponding to the action spectrum of the photovoltaic devices were calculated and are shown in Fig. 6. The PEOPT/ C_{60} interface of bilayer structures of PEOPT/ C_{60} on SiO_2/Si substrates was also studied with spectroscopic ellipsometry, and the interface was found to be sharp with no mixing of the two materials. The optical function of PEOPT shows an extinction coefficient with maximum at 475 nm (2.61 eV), which corresponds to a maximum in absorption at 468 nm (2.65 eV) as given by Eq. (23). The onset of absorption is at about 620 nm (2.00 eV). In the case of C_{60} , the onset for absorption is at about 725 nm (1.71 eV) with a rather sharp peak in the extinction coefficient at 345 nm (3.59 eV) and broader features with peaks at 447 nm (2.77 eV), and 611 nm (2.03 eV), respectively. It should also be noted that there is a shoulder at about 490 nm (2.35 eV) and also a small shoulder at about 670 nm (1.85 eV). The result for the optical function of thin films of C_{60} is in good agreement with previous reported results.^{17–19}

With the use of the optical functions presented in Figs. 4 and 5 and those obtained for the other materials inside the

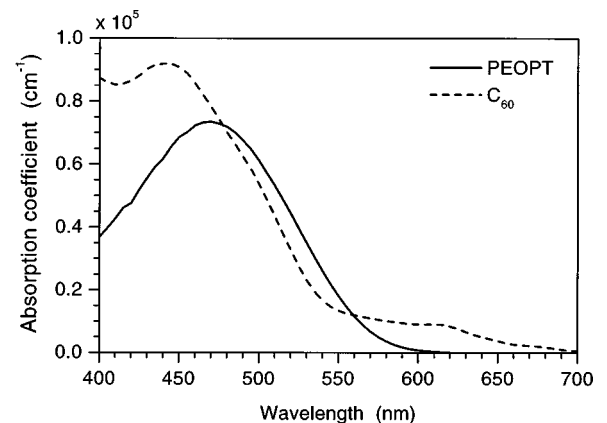


FIG. 6. The absorption coefficient ($\alpha = 4\pi\eta/\lambda$) of PEOPT (solid line) and C_{60} (dashed line) in the wavelength range corresponding to the action spectrum of the photovoltaic devices.

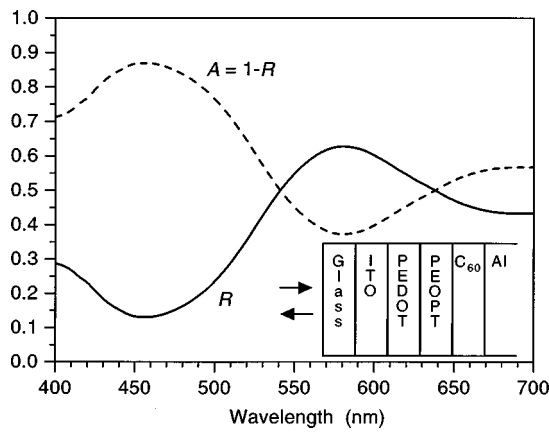


FIG. 7. Calculated reflection R and absorption $A=1-R$ from a glass (1 mm)/ITO (120 nm)/PEDOT (110 nm)/PEOPT (40 nm)/ C_{60} (35 nm)/Al device, which is schematically presented in the lower right corner.

device, the intensity (energy) reflectance can be calculated. The reflectance is given as $R=|r|^2$, where r is given by Eq. (9). In Fig. 7, the calculated reflectance of a glass (1 mm)/ITO (120 nm)/PEDOT (110 nm)/PEOPT (40 nm)/ C_{60} (35 nm)/Al device is presented. Since the Al layer is much thicker than the penetration depth of light at these wavelengths, the total light absorption in the device is described by $1-R$, which is also presented in the same figure. The $1-R$ also represents the upper limit for the fraction of incident photons at the device that can contribute to the photocurrent. Concomitantly, this must also be the upper limit for the photon to current collection efficiency of this particular device. In this case we obtain a maximum of absorption at about 460 nm where about 87% of the incident photons are absorbed in the device. If all the absorbed photons in the device would contribute to the photocurrent, we would obtain a photon to current collection efficiency of 87%, which, of course, is not the case. However, this is of importance in the evaluation of the design of the device.

The generation of photoexcited species at a particular position inside the thin film structure was in Sec. IIIB shown to be proportional to the product of the modulus squared of the electric field, the refractive index, and the absorption coefficient. Thus, the excitation distribution in fact is discontinuous at the interfaces since both refractive index and extinction coefficient changes at the interface. The calculated distribution of the normalized modulus squared of the incident optical electric field for two device structures with two different C_{60} layer thickness (35 and 80 nm) for $\lambda=460$ nm is presented in Fig. 8. It is seen that $|E|^2$ is strongly influenced by interference effects, which gives rise to a varying value in the device. The C_{60} /Al interface is the most dominant boundary condition inside the device and is therefore also to a large extent determining the distribution inside the device. The active interface in the device is the PEOPT/ C_{60} interface, which acts as a dissociation site for excitons. Due to the limited diffusion range of the excitons, only those excitons that reach the dissociation site will contribute to the photocurrent. Thus, in order to maximize the number of excitons at this interface, we are interested in maximizing the modulus squared of the electric field at this interface. As

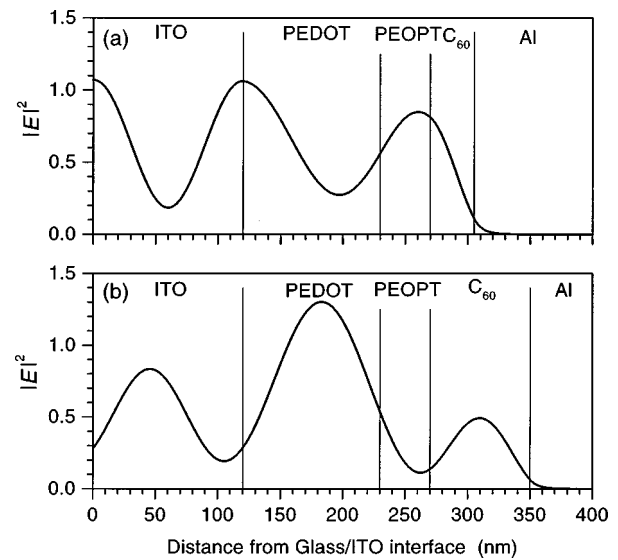


FIG. 8. Calculated distribution of the normalized modulus squared of the optical electric field $|E|^2$ inside a photovoltaic device: glass (1 mm)/ITO (120 nm)/PEDOT (110 nm)/PEOPT (40 nm)/ C_{60} /Al with a C_{60} layer thickness of (a) 35 nm and (b) 80 nm for a wavelength of 460 nm.

seen in Fig. 8, the value of $|E|^2$ at this interface for different thickness of the C_{60} layer is very different. In Fig. 9, the normalized modulus square of the electric field at the PEOPT/ C_{60} interface for a wavelength of 460 nm and for two different thicknesses of the PEOPT layer is plotted versus thickness of the C_{60} layer. A global maximum at about 35 nm for the C_{60} layer thickness indicates that this is an optimal choice in order to maximize the photocurrent efficiency at this wavelength. It is important to note that this only holds for this wavelength, but this analysis still can be used in order to maximize the peak efficiency of the device by choosing the correct thickness at the proper wavelength. Others¹¹ have also used the C_{60} layer as a spacer layer to increase the optical electric field at the heterojunction in order to enhance the photovoltaic efficiency. With thorough knowledge about the optical properties of the materials in-

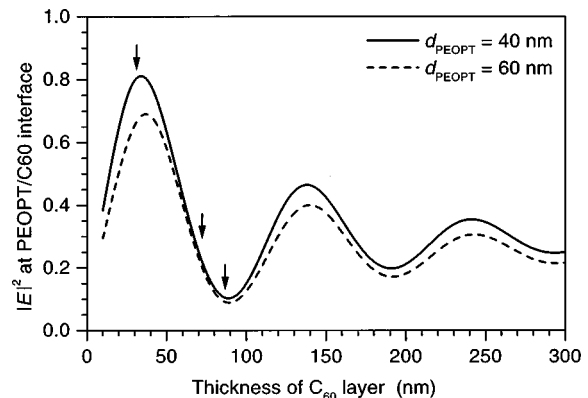


FIG. 9. Calculated value of the normalized modulus squared of the optical electric field $|E|^2$ at the PEOPT/ C_{60} interface inside a photovoltaic device, glass (1 mm)/ITO (120 nm)/PEDOT (110 nm)/PEOPT (40 nm)/ C_{60} /Al, versus thickness of the C_{60} layer for a wavelength of 460 nm. Arrows mark 31, 72, and 87 nm thickness of the C_{60} layer, corresponding to photovoltaic devices having their experimental IPCE shown in Fig. 11.

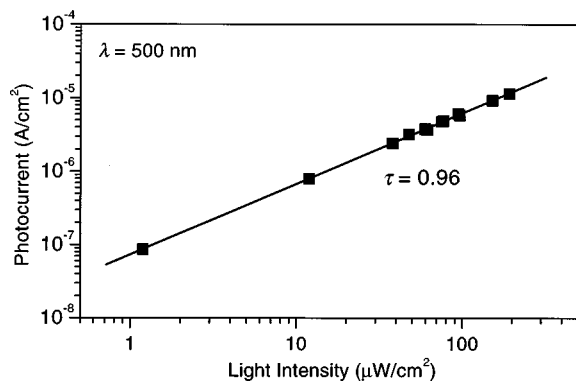


FIG. 10. Measured photocurrent vs intensity of light at a wavelength of 500 nm incident at a photovoltaic device: glass (1 mm)/ITO (120 nm)/PEDOT (110 nm)/PEOPT (40 nm)/C₆₀ (32 nm)/Al.

cluded in the device, a much more detailed and fundamental analysis can be performed. However, a more correct way to optimize the efficiency of the device for its whole action spectrum and not only one wavelength is to consider the total efficiency of the device, by integrating the efficiency for all wavelengths in the action spectrum of the device and maximizing the integrated value.

Experimental data of photocurrent versus intensity of the incident light at one wavelength for a glass (1 mm)/ITO (120 nm)/PEDOT (110 nm)/PEOPT (40 nm)/C₆₀ (32 nm)/Al device, representative for the devices studied in this work, is shown in Fig. 10. Similar results were obtained for other wavelengths. According to Eqs. (34) and (36) there should be a linear dependence between the photocurrent and intensity of the incident light, that is, $J_{\text{photo}} \propto I_0^\tau$, where $\tau = 1$. The light intensity dependence of the photocurrent as described by the value of the photocurrent-light exponent τ are related to the efficiency of the generation and dissociation of the excitons and the electrical characteristics of the photovoltaic device. As seen in Fig. 10, there is a linear dependence between the photocurrent and intensity for the studied devices, with the photocurrent-light exponent very close to unity as an indication of the validity of the assumptions used in the modeling of the experimental photocurrent action spectra (see Sec. III A).

The efficiency of a photovoltaic device can be described by the incident monochromatic photon to current collection efficiency (IPCE), which gives us the ratio between the number of generated charge carriers contributing to the photocurrent and the number of incident photons. The IPCE, in percent, is given as

$$\text{IPCE}(\%) = 1240 \times \frac{J_{\text{photo}}}{\lambda I_0}, \quad (37)$$

where J_{photo} is the short-circuit current ($\mu\text{A}/\text{cm}^2$), I_0 and λ are the intensity (W/m^2) and the wavelength (nm), respectively, of the incident light. In the IPCE value the photocurrent is normalized by the intensity of the incident light which therefore is eliminated from Eqs. (34) and (36) when calculating the modeled photocurrent action spectrum. The calculated short-circuit photocurrent action spectra were fitted to the experimental data with the Gauss-Newton algorithm by

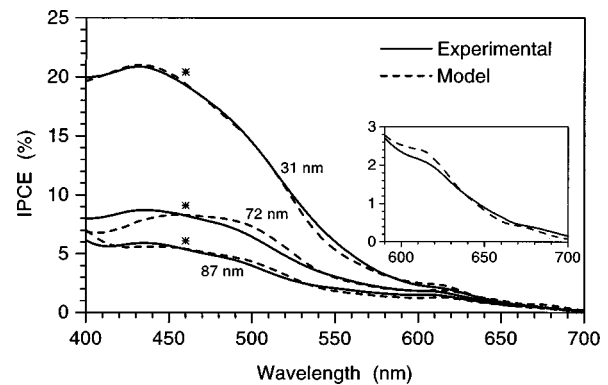


FIG. 11. Experimental incident monochromatic photon to current collection efficiency IPCE action spectra (solid line) of a glass (1 mm)/ITO (120 nm)/PEDOT (110 nm)/PEOPT (40 nm)/C₆₀/Al devices with different thickness of the C₆₀ layer and the best fit from model (dashed line). The stars (*) mark the wavelength corresponding to the prediction of the model in Fig. 9. In the inset a magnification of experimental and model data in the wavelength range 590–700 nm for the device with a 31 nm thick C₆₀ layer are shown.

varying the thickness of the C₆₀ layer and the diffusion ranges of the PEOPT and C₆₀ in order to obtain a best fit of model data to multiple sets of experimental data. To model the experimental short-circuit photocurrent action spectra, it was not sufficient only to use contributions to the photocurrent from the polymer to obtain a good fit. Thus, contributions from the C₆₀ layer to the photocurrent were also included in the modeling to obtain a reasonable fit of model data to experimental data. For that reason and assumption (5), stated in Sec. III A, both the PEOPT/C₆₀ interface and the C₆₀/Al interface were acting as dissociation sites for the excitons created in the C₆₀. At these dissociation sites the total quantum efficiency of the free charge generation was assumed to be unity. Figure 11 shows experimental IPCE curves for three devices with different thickness of the C₆₀ layer, 31, 72, and 87 nm, respectively. As can be seen in the experimental IPCE curves they have a similar shape but with quite a different absolute value. Arrows in Fig. 9 mark the thickness of the C₆₀ layers corresponding to these values. The most efficient device has a C₆₀ layer thickness of 32 nm, which is very close to the optimal thickness as described previously. Also, there is a photocurrent above the absorption edge of PEOPT (620 nm) indicating a contribution from the C₆₀ to the photocurrent. This is also supported by the small peak/shoulders at about 610 and 670 nm, see the inset of Fig. 11, which were found as a peak and a shoulder at the same position in the extinction coefficient of C₆₀. Also included in the graph is a best fit of modeled data from a data analysis where model data were fitted to the three data sets simultaneously. The advantage of fitting multiple data sets simultaneously is the parameters such as the diffusion range of PEOPT and C₆₀ are assumed to be the same for all three data sets and independent of the energy with which the excitons were created. In this way the correlation between the diffusion range of PEOPT and C₆₀ and the C₆₀ layer thickness, which are the parameters varied in the fit, decreases and the confidence in the fit is increased. The data fit shows a very good agreement between model and experimental data

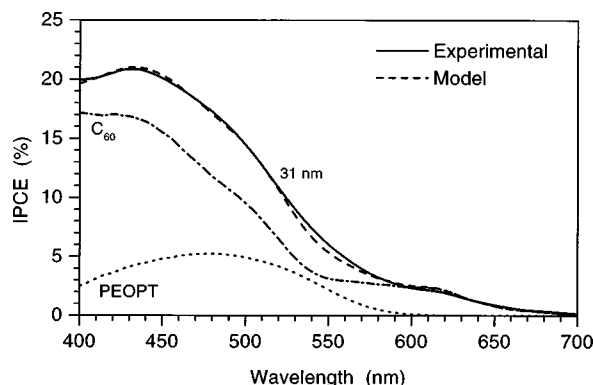


FIG. 12. Experimental and calculated incident monochromatic photon to current collection efficiency, IPCE, action spectra, and the contribution from the PEOPT and C_{60} layer, respectively, as obtained in the model.

resulting in diffusion ranges of 4.7 nm for PEOPT and 7.7 nm for C_{60} . These diffusion ranges seem to be quite small but for PEOPT diffusion ranges of the same order which have been obtained in photoluminescence studies.²⁰ Moreover, in Fig. 11 stars (*) mark the wavelength ($\lambda = 460$ nm) corresponding to the model prediction in Fig. 9. The IPCE value at this wavelength is 19.3%, 8.2%, and 5.4% for the 31, 72, and 87 nm thick C_{60} layer, respectively. In order to see the different contributions to the photocurrent from the PEOPT and C_{60} layer, respectively, Fig. 12 shows the experimental data and best model fit data for the device with 31 nm C_{60} layer thickness together with these contributions. Rather unexpected is that the largest contribution to the photocurrent comes from the C_{60} layer and only a smaller part is due to the PEOPT over the total spectral range. Below the absorption edge of PEOPT the total contribution is from the C_{60} as expected. The same relation between the PEOPT and C_{60} contributions is also valid for the different thicknesses of the C_{60} layer. We also note that it was possible to obtain reasonable good fit of model data to experimental data by only considering the contribution from the PEOPT/ C_{60} interface, omitting the C_{60} /Al interface. The obtained exciton diffusion ranges became in this case almost the same for PEOPT (5.4 nm) but about twice for the C_{60} (14.1 nm), and with the drawback that the obtained thicknesses of the C_{60} layers showed a larger deviation from those obtained by measurements using ellipsometry than in the case above. Diffusion ranges for C_{60} are unfortunately not available for comparison. However, the contributions to the photocurrent from the PEOPT relative to the C_{60} layer were the same as those shown in Fig. 12.

The generation of photocurrent at polymer/ C_{60} junctions has been attributed solely to excitations inside the polymer phase in previous experimental work.^{11,12,21,22} We note, however, that the spectral distribution of photocurrent generation in C_{60} ²³ and in PPV/ C_{60} systems²⁴ shows the same small bumps/shoulders at the energies at about 610 nm (2.03 eV) and 670 nm (1.85 eV) as we observe in these systems; we also observe them in various polymer blend/ C_{60} double layer devices.^{25,26} In all polymer/ C_{60} double layer devices studied so far, we also observe the dramatic enhancement of quantum efficiency in the blue range of wavelengths, an ultraviolet

anomaly that cannot be directly understood from the polymer absorption. We consider both of these experimental effects to be caused by absorption in the C_{60} solid, and provide direct evidence for photocurrent generation from the fullerene layer.

Photoconductivity in C_{60} layers has been observed before, and the origin of such photoconductivity in terms of electron-hole pair generation or exciton generation has been discussed. More important are the theoretical studies of the excitations of polymer donor/(molecular/polymer) acceptor.^{27,28} The presence of photoinduced electron transfer in such structures has been modeled as a decay of an exciton located on the polymer into a continuum-like charge transfer excitation. Within the modeling of Rice-Gartstein,²⁷ no account is given of the case of a photoexcited acceptor transferring a hole to the polymer donor.

Our modeling has been based on the assumption that the photocurrent generation occurs by diffusion of the excited state to do charge transfer at the polymer/ C_{60} interface. We extract values of 4.7 nm for this diffusion length and are then seriously concerned with the validity of the model. This length corresponds to 10–12 monomer units of polythiophene, which is only slightly longer than the length of the diffusing object—which makes diffusion a suspicious terminology.

We consider that our results imply that the excited state leading to charge generation can also be created by optical absorption in the donor. This is consistent with the suggestion by Vacar and Heeger that the excited state leading to charge transfer is distributed over a long distance and extending deep into the polymer layer;²⁹ only now we must also consider the inclusion of the C_{60} layer in the modeling. The nature of this delocalized state, which must be assumed to extend over the polymer/ C_{60} junction, is not known. Another probe of this effect is through the disappearance of luminescence due to formation of charge transfer states. Experiments on the photoluminescence quenching in polymer/ C_{60} contacts—a photoluminescence solely generated from the polymer—are presently in progress and indicate that the active layer close to the polymer/ C_{60} junction is of similar thickness to that of the diffusion length of excitons here deduced.²⁰ No photoluminescence is available to probe this effect on the C_{60} side.

In this modeling no considerations of the electrical properties of the device were taken. This means that we assume all generated charge carriers to contribute to the short-circuit photocurrent. Although this assumption is not correct, the modeling of the distribution of the optical electric field and its influence on the short-circuit photocurrent action spectra are important factors to take into account in the construction of photovoltaic heterojunction devices. However, in order to obtain a correct description of the behavior of this type of device, the electrical properties of the device should also be included in the model.

Finally, we note that the reflectance predicted for the thin film device puts an upper limit to the absorption in active materials, and we can therefore estimate the internal quantum efficiency with the ratio between experimentally observed IPCE divided by the absorption in the device. This

can reach as high as 25% in the blue range for the optimized geometry.

V. CONCLUSIONS

We have modeled the experimental action spectra of a thin film photovoltaic device consisting of a heterojunction between a polythiophene and fullerene. The model is based on the assumption that photocurrent generation is the result of generation and diffusion of photogenerated species (excitons), which are dissociated by charge transfer at the heterojunction. In the model, the optical electric field distribution inside the photovoltaic device is of fundamental importance and is important to consider, especially for a device with a highly reflecting metal electrode present. In order to obtain a good agreement between model and experimental action spectra, photocurrent generation from both the polymer and the fullerene layer was needed. By utilizing a regression analysis where physical model parameters were adjusted, a best fit of model data to multiple sets of experimental data was obtained. Resulting values of the exciton diffusion range of PEOPT (4.7 nm) and C₆₀ (7.7 nm) were determined, which clearly indicate that the diffusion ranges of the photoactive materials limit the efficiency of the device. Photoinduced charge transfer states generated at the polymer/C₆₀ contact can be elucidated from photocurrent generation via absorption both in the polymer and the C₆₀ layer. Quantum chemical modeling of these phenomena could help resolve these issues.

ACKNOWLEDGMENTS

The authors acknowledge the financial support of the Swedish Research Council for Engineering Sciences, and the Göran Gustafsson Foundation. The polymer PEOPT was synthesized by W. Mammo, M. R. Andersson, and co-workers at Chalmers University of Technology, Sweden. M. Theander, Linköping University, is acknowledged for valuable discussions.

¹L. S. Roman, W. Mammo, L. A. A. Pettersson, M. R. Andersson, and O. Inganäs, *Adv. Mater.* **10**, 774 (1998).

- ²M. Granström, K. Petritsch, A. C. Arias, A. Lux, M. R. Andersson, and R. H. Friend, *Nature (London)* **395**, 257 (1998).
- ³L. S. Roman, M. R. Andersson, T. Yohannes, and O. Inganäs, *Adv. Mater.* **9**, 1164 (1997).
- ⁴A. K. Ghosh and T. Feng, *J. Appl. Phys.* **49**, 5982 (1978).
- ⁵J. Wagner, T. Fritz, and H. Bötcher, *Phys. Status Solidi A* **136**, 423 (1993).
- ⁶A. Désormeaux, J. J. Max, and R. M. Leblanc, *J. Phys. Chem.* **97**, 6670 (1993).
- ⁷C. W. Tang and A. C. Albrecht, *J. Chem. Phys.* **62**, 2139 (1975).
- ⁸A. K. Ghosh, D. L. Morel, T. Feng, R. F. Shaw, and C. A. Rowe, Jr., *J. Appl. Phys.* **45**, 230 (1974).
- ⁹H. B. DeVore, *Phys. Rev.* **102**, 86 (1956).
- ¹⁰M. G. Harrison, J. Grüner, and G. C. W. Spencer, *Phys. Rev. B* **55**, 7831 (1997).
- ¹¹J. J. M. Halls, K. Pichler, R. H. Friend, S. C. Moratti, and A. B. Holmes, *Appl. Phys. Lett.* **68**, 3120 (1996); *Synth. Met.* **77**, 277 (1996).
- ¹²N. S. Sariciftci, D. Braun, C. Zhang, V. I. Srdanov, A. J. Heeger, G. Stucky, and F. Wudl, *Appl. Phys. Lett.* **62**, 585 (1993).
- ¹³S. Morita, S. B. Lee, A. A. Zakhidov, and K. Yoshino, *Mol. Cryst. Liq. Cryst. Sci. Technol., Sect. A* **256**, 839 (1994).
- ¹⁴G. E. Jellison, Jr., *Thin Solid Films* **234**, 416-422 (1993).
- ¹⁵Z. Knittl, *Optics of Thin Films* (Wiley, London, 1976).
- ¹⁶R. M. A. Azzam and N. M. Bashara, *Ellipsometry and Polarized Light* (North-Holland, Amsterdam, 1977).
- ¹⁷A. Richter and J. Sturm, *Appl. Phys. A: Mater. Sci. Process.* **61**, 163 (1995).
- ¹⁸P. Milani, M. Manfredini, G. Guizzetti, F. Marabelli, and M. Patrini, *Solid State Commun.* **90**, 639 (1994).
- ¹⁹M. S. Dresselhaus, G. Dresselhaus, A. M. Rao, and P. C. Eklund, *Synth. Met.* **78**, 313 (1996).
- ²⁰M. Theander *et al.* (unpublished).
- ²¹N. S. Sariciftci and A. J. Heeger, in *Handbook of Organic Conductive Molecules and Polymers*, Volume 1, edited by H. S. Nalwa (Wiley, New York, 1997), pp. 413-455.
- ²²A. Fujii, A. A. Zakhidov, V. V. Borovkov, Y. Ohmori, and K. Yoshino, *Jpn. J. Appl. Phys., Part 2* **35**, L1438 (1996).
- ²³N. Minami, S. Kazaoui, and R. Ross, *Mol. Cryst. Liq. Cryst. Sci. Technol., Sect. A* **256**, 233 (1994).
- ²⁴J. J. M. Halls, Ph.D. thesis, Cambridge University, 1997.
- ²⁵L. Chen, L. S. Roman, D. M. Johansson, M. R. Andersson, and O. Inganäs, (unpublished).
- ²⁶L. Ding *et al.* (unpublished).
- ²⁷M. J. Rice and Y. N. Gartstein, *Phys. Rev. B* **53**, 10764 (1996).
- ²⁸A. Köhler, D. A. dos Santos, D. Beljonne, Z. Shuai, J.-L. Brédas, A. B. Holmes, A. Kraus, K. Müllen, and R. H. Friend, *Nature (London)* **392**, 903 (1998).
- ²⁹D. Vacar, E. S. Maniloff, D. W. McBranch, and A. J. Heeger, *Phys. Rev. B* **56**, 4573 (1997).